

Mechanistic insights of key host proteins and potential repurposed inhibitors regulating SARS-CoV-2 pathway

Debabrata Pramanik^{1,+}, Aiswarya B Pawar^{2,+}, Sudip Roy^{*2} and Jayant Kumar Singh^{*1,2}

¹Department of Chemical Engineering
Indian Institute of Technology, Kanpur, India

²Prescience Insilico Private Limited
Old Madras Road, Bangalore 560049, India

*Corresponding authors: Sudip Roy (sudip@prescience.in) and Jayant Kumar Singh (jayantks@iitk.ac.in)

+These authors contributed equally.

ABSTRACT

The emergence of pandemic situations originated from SARS-CoV-2 and its new variants created worldwide medical emergencies. Due to the non-availability of efficient drugs and vaccines, hundreds of thousands of people succumbed to death intoxicated by this virus. At these emergency hours, repurposing existing drugs can effectively treat patients critically infected by SARS-CoV-2. Using a high-throughput screening approach, we validated a list of potential repurposed drugs, like Nafamostat, Camostat, Sunitinib, Valproic acid, Zotatifin, and essential host target proteins HDAC2, eIF4E2, CSK22, that are essential for viral mechanism. We determined multiple dissociation pathways of repurposed drugs, suggesting the availability of sub pockets within the host target proteins. We showed the preferential residues involved in the (un)binding kinetics of

the ligands correlated to the underlying mechanism of the host protein activity. Interestingly, the residues we obtained for HDAC2 and CSK22 target proteins, which we highlighted, are also involved in the catalytic activity. The mechanistic insight presented in this work is envisaged to help use these key host proteins and potential repurposed drugs as a treatment for the SARS-CoV-2 virus.

Introduction

Over the past two decades, the virus that causes coronavirus disease has turned out to be lethal across the world. Earlier it was considered as a mild disease infecting immunocompetent people. Over the years, the virus has evolved into being fatal, with a higher transmissibility rate. Severe Acute Respiratory Syndrome (SARS-CoV-2) [1], the virus that causes COVID-19, has become the worst and uncontrollable public health crisis in a century. After the first outbreak, the virus mutated into more infectious variants, triggering multiple pandemic waves. The pandemic second wave has already shown to be aggressively targeting the younger population. Unlike the first wave, 60-70% of the infected people in the second wave required critical care and hospitalization. A statement released by the Centers for Disease Control and Prevention (CDC) in July 2021 claimed that the Delta variant has the highest spread cases and severe outcomes even among vaccinated people. The Delta variant has shown to be twice as powerful as previous variants, but further details are still not understood. Generally, on-set of infection, a person can experience milder flu-like symptoms [2,3], further developing into more acute severe respiratory failure [4] and other multi-organ complications. In this emergency, many repurposing drugs have been applied for COVID-19 treatment, although the FDA does not yet approve them.

Researchers are scrambling to unravel how the virus hijacks the host and eventually affects the host regulatory mechanism. The viral genome is complex and encodes structural and non-structural proteins [5,6]. The viral proteins utilize the host proteins from their entry to transmission within host cells for their life cycle [7,8]. Identifying virus-host protein interactors in the complex pool of sequential pathways is vital to study the viral pathogenesis and host tolerant environment for viruses. In particular, the Delta variant with multiple mutations in the spike protein binds to the host angiotensin-converting enzyme 2 (ACE2) [9] receptor, which is present outside the human throat and lung cells, 2-4 times stronger. Recent proteomics approaches have revealed that viral proteins can enhance or lower the activity of hundreds of human kinases involved in cellular activities and immune response [10]. So, the possibility of targeting pro-viral cellular signaling could make the host immune system resistant to viral replication. It is crucial when the host has antibodies developed for SARS-CoV-2 by vaccination or recovery from COVID-19 infection and is still susceptible to new variants [11].

The Caesin Kinase 2 (CK2) [12,13], Histone deactylease (HDAC2) [14,15], and eIF4E2 host proteins are essential for the normal functioning of cells, involved in cell cycle checkpoints, metabolic pathways, epigenetic regulators, mRNA translation pathways. These proteins get perturbed in the cancerous cells. Previous experimental studies have highlighted that cancer cells and viral pathogens follow similar molecular mechanisms for apoptosis and evade host immune response. Coronaviruses take over these machinery pathways. For example, viral protein Nsp1 recruits the host proteins and reduces the overall host protein translation in the cell by 70% [16].

Recent mass-spectrometric experiments reported that an entry of a virus to the host target induces a significant change in protein phosphorylation and disrupts the host cytoskeletal organization by upregulating the CK2 kinases activity [17]. Additionally, pharmacological studies in human cell

lines have indicated the drug Silmitasertib (currently in phase 2 trials) to have high inhibitory activity of CK2 kinases, suggesting the role of these kinases in the SARS-CoV-2 life cycle [17]. Furthermore, Senhwa Biosciences get approval from Independent Data Monitoring Committee (DMC) for severe COVID-19 patients. Previous studies [18–20] on SARS-CoV have shown that drugs Nafamostat [18,19] and Camostat [21] are potential candidates to stop viral entry by binding to transmembrane protease serine 2 (TMPRSS2) proteases [22–24]. However, even at higher concentrations, Camostat showed 65% inhibition of protease binding, and 35% virus entry takes place via the endosomal cathepsin pathway [25]. Although, the role of these drugs on intracellular proteins that help regulate viral protein processing is still not clear. Similarly, the Zotatfin drug has shown to be effective in the translation machinery of the host, where viruses rely on host-dependent mRNA translation. Repurposing of these drugs can be an effective way in terms of cost and time for treating COVID-19.

Our recent study [26] followed an exhaustive screening of FDA-approved drugs against multiple host targets by using high throughput computational screening platform [27] utilizing molecular docking, all-atom molecular dynamics simulations including solvent and state of the art free energy calculations. The multi-target multi-ligand enhanced sampling approach provides highly selective off-target drug combinations with stable affinities. Interestingly, we found drugs that have high binding free energies were already in the clinical trial phase for COVID-19. Especially the drug Silmitasertib targeting CK2, which showed good binding free energies in our previous work [26], is already in phase II clinical trials. Similarly, the drug Zotatfin targeting the eIF4E elongation factor is in clinical trial phase I. We found that some off-targets showed good binding free energies but have not been previously explored experimentally [28]. However, thermodynamics and kinetics are essential in the early stages of rational drug design, but molecular

determinants could describe the modulation of binding and unbinding kinetics and disclosing their pathways [29]. In this paper, we have considered the targets and off-targets combinations [30] having good binding free energies and subjected to performing a combined all-atom molecular dynamics and enhanced sampling simulations. We explore the dissociation pathways of the drugs from the host-target proteins by considering the essential interacting residues involved in (un)binding processes. The information obtained from this study will further help in enhancing our knowledge on drug target mechanisms and design better therapeutics.

Computational methodologies

We applied a rigid docking protocol to generate the docked complex using the Autodock suite (Autodock 4.2.6) [31]. We performed docking on the crystal structures of the proteins (Table 1), and if any missing loops were present have been modeled using Modeller (Modeller 9.24) [32]. We first obtained minimum energy structures for proteins and ligands (Figure 1) followed docking to perform docking. The docking sites have been selected by either using the inhibitor-bound position in the crystal structure or finding the binding sites using the Autoligand tool [33]. We took the conformation corresponding to the minimum docking score for all-atom molecular dynamics (MD) using GROMACS-2018 [34]. Charmm27 force field parameters with cmap corrections have been used to model bonded, nonbonded interactions for protein [35]. To generate ligand interaction parameters, we optimized the ligands' geometry employing GAUSSIAN 09 [36] using a semi-empirical method at the PM6 level, followed by density functional theory (DFT) optimization using M06 functionals and 6-311g (d,p) basis sets. To account bulk solvent effect, we employed the PCM method. The partial charges have been calculated using the CHELPG method [38] on

this DFT-optimized structure. Following this, we used the swissparam web service [37] to obtain charmm compatible parameters. The obtained docked complex was solvated in TIP3P water followed by added Na⁺, Cl⁻ ions to neutralize the system. Periodic boundary conditions were applied in all directions to mimic the bulk property. After setting up the initial system, we performed energy minimization using the steepest descent method to remove the bad contacts of the solute due to overlap with the water molecules. It was followed by NVT equilibration for a duration of 500 ps at 300 K using a modified Berendsen thermostat [39]. Later, a 1 ns NPT equilibration was followed after NVT at atmospheric pressure using Parrinello-Rahman [40] barostat. The Particle-Mesh Ewald (PME) [41] method has been employed to calculate the long-range electrostatic interaction, and the short-range interactions were calculated using a 1 nm cut-off. The LINCS algorithm [42] has been used to choose 2 fs integration time steps. We performed a 100 ns production run in the NPT ensemble for all the systems using this protocol. We analyzed these trajectories and calculated the bound state properties of the protein-ligand systems. We calculated the contact frequency between the protein and ligand to extract the crucial residues involved in the interaction at the bound state, considering the minimum distance criterion choosing a cut-off of 0.4 nm. Further, we pulled out the interaction fingerprint for the selective protein residues (i.e., that remain in contact for more than 75 % of simulation time) obtained from the contact frequency [43].

To explore the ligand dissociation [29,44–47] from the protein binding pocket, we employed metadynamics (metaD) [48] and its variant well-tempered metadynamics (wt-metaD) [49] using PLUMED 2.5.4 [50] and GROMACS 2018 [34]. In a metaD simulation, a history-dependent bias is deposited sequentially, prohibiting the system from revisiting already visited portions in the phase space. Thus eventually, the system escapes from the minimum in the energy landscape to

the aqueous medium. In wt-metaD, the height of the deposited bias is gradually decreased to have better and quicker convergences of the system. The final equilibrium coordinates from the MD simulation were taken as the initial structures in wt-metaD simulations. In a metaD or wt-metaD simulation, the bias is added to the system along a reaction coordinate. A good reaction coordinate will have the following two criteria: (i) it should show a timescale separation between the slowest motion in the system with that of the fastest motion, and (ii) it should be able to demarcate all the relevant metastable states. Here we take distance (between the center of masses of the ligand heavy atoms and the center of masses of the protein binding pocket) as the reaction coordinate (RC). Once the simulation converges, the unbiased Boltzmann distribution of the RC is extracted by adding the deposited hills. The following biasing parameters have been used in wt-metaD simulations: bias deposition frequency of 500 steps (1 ps), gaussian hill height 1.5 – 2.0 kJ/mol, hill width 0.02 - 0.1 nm, bias factor 10 – 15, temperature 300 K. For each system we performed 10 independent wt-metaD simulations starting from a new initial configuration. To calculate the average free energy, we first calculated independent probability, then averaging over probabilities followed by averaged free energy [26,51].

First, to calculate the dissociation rate, we calculate the residence time over 10 trajectories for a system. We calculate the accelerated time or residence time by multiplying the biased time with the acceleration factor and obtain the average residence time after averaging over independent values. Further to explore the crucial protein residues while dissociating the ligand from the binding pocket, we calculated the minimum distance between the ligand heavy atoms and protein residues of the system and repeated this exercise for all 10 independent runs, as shown in Figure S2. Following this, we extracted only those specific residues of the protein for which, at least for a run, it has a minimum ligand and protein residue distance < 0.2 nm (shown in Figure S3). Then

we calculated the normalized probabilities for these specific residues for the distance between the residues and the ligand heavy atoms and repeated this exercise for all six systems as shown in Figure S4-S9.

Results and discussion

Silmitasertib, Zotatfin showed high binding free energies with CK2 and eIF4E proteins in clinical trials for COVID-19 (NCT04668209, NCT04632381). In addition, we identified drugs that potentially interact with one or more off-targets with higher affinities. On-set of infection, the proteins associated with transcription, translation mechanisms are expressed. So, it is advantageous to use drugs that can target multiple host proteins at different stages of the mechanism. Such off-target combinations, eIF4E2 with Nafamostat, Camostat, and HDAC2 with Valproic acid, Nafamostat having good binding affinities, are listed in Table 2.

Conformational stability of the host target - drug complexes

We performed atomistic molecular dynamics simulations on six drug-protein combinations (Table 1) to provide time-dependent changes. We calculated the backbone Root Mean Square Deviation (RMSD) and Root Mean Square Fluctuation (RMSF) to evaluate the conformational stability. Figure 2 and Figure 3 show the RMSD and RMSF of different targets bound to Nafamostat, Camostat, Zotatfin, Silmitasertib, and Valproic acid. In all cases, the RMSD was less than 0.45 nm suggesting the conformation over 100 ns has been less deviated and stable. The eIF4E2-Zotatfin and CSK2-Silmatersitib complexes showed more stable conformations ranging between 0.2 - 0.25 nm.

Additionally, the HDAC2 protein complex with Nafamostat and Valproic acid displayed a stable conformation with a value less than 0.15 nm for the first 50 ns. The values deviated after 50 ns, but still, conformations remained within the stable range of 0.2 - 0.25 nm. The eIF4E2-Camostat complexes showed the highest deviations for the rest of the complexes. It shows the highest variation at 50 ns and 75 ns. To understand protein regions that contribute to the conformational changes or stability, we calculated the RMSF at the residue level. The mobility of residues was observed for all six drug-protein combinations, as shown in Figure 3. The high fluctuations observed on the terminal ends of proteins can be neglected due to their high mobility. Overall, fewer residue-level fluctuations were observed for all six candidates, suggesting stable nature. However, high fluctuations were observed in HDAC2 PHE210 residue in both Nafamostat and Valproic acid. The PHE210 residues are conserved and present at the gateway of the binding pocket of HDAC2 proteins and selectively interact with ligands.

Preferential binding sites for drug-host target proteins

To further understand the molecular details of the protein-drug interactions in a bound state, we calculated the minimum distance between them, as shown in Figure 4. It was interesting to see crucial residues involved in the interactions that remain in contact for more than 75% of the simulation time (shown in Table S1). In the eIF4E translation factor, the residues THR29, SER30, SER31, TRP80 were shown to interact with Nafamostat, Camostat, and Zotatfin. However, ILE177, MET179, and PRO180 are present in Camostat and Zotatfin and not in Nafamostat. Similarly, for the HDAC2 epigenetic factor, the residues that interact with Nafamostat and Valproic acid were quite similar. The residues interacting are TYR29, MET35, PRO37, ARG39,

ILE40, PHE114, ALA141, GLY142, LEU144, CYS156, GLY305. Interestingly, HIS183 was shown to be interacting with Nafamostat and not Valproic acid. For CK2-Silmitasertib, the residues LEU46, GLY47, ARG48, GLY49, VAL54, VAL60, LYS69, ILE96, PHE114, ILE117, ASN119, MET164, ILE175, ASP176 were shown to interact in the bound state.

We calculated interaction fingerprints in a binary vector to further understand the nature of intermolecular interactions between the target proteins and drugs that remain in contact for more than 75% of simulation time. The knowledge of interactions in terms of Hydrogen-bonding, Hydrophobic interactions, and $\pi - \pi$ stacking and their conformations was considered for protein-drug. Figure 5 shows the interaction fingerprints for the eIF4E translational factor. THR29, SER31, TRP80, and PRO180 residues were observed in all three drug complexes involved in hydrophobic interactions. The TRP80 is also shown to form $\pi - \pi$ stacking interaction. In Nafamostat and Camostat, SER31 has also been observed to form transient hydrogen bonding. Interestingly, ILE177 and MET179 are involved in hydrophobic interactions in Camostat transiently and Zotatfin continuously. Similarly, in Figures 6 (a) and (b), the HDAC2 residues TYR29, MET35, ARG39, ILE40, ALA141, GLY143, LEU144, CYS156, GLY305 form hydrophobic interactions with the drug Nafamostat and Valproic acid. There was a transient hydrogen bonding interaction with residues ARG39 in both and TYR308 in Nafamostat and GLY294 in Camostat. We observed the $\pi - \pi$ interactions only in Nafamostat at residues HIS134, HIS135. In CK2-Silmitasertib, the hydrophobic interactions were observed with LEU46, GLY47, ARG48, GLY49, VAL54, LYS69, ILE196, PHE114, ILE117, ASN119, MET164, ILE175, ASP176. At the start of the simulations, we observed transient hydrogen bonds in LYS69 and ASP176, lost towards the end of the simulations. We noticed $\pi - \pi$ interactions to be formed by PHE114 at the start of the simulations.

Correlation between thermodynamics and kinetics of drug-target combinations

Further, to correlate the host target-drug complexes' thermodynamic behavior and kinetics, we calculated free energy barriers and dissociation rates, as shown in Table 2. Figure 7 shows the "log(K_{off})" vs "free energy barrier (ΔG)" plot for all the drug-target combinations studied and discussed above. For better efficacies of drug molecules, the free energy barriers are suggested to be high, and the rate of dissociation of the drugs is proposed to be low and vice versa. We observe that for systems with higher free energy barriers (low values of ΔG), log(K_{off}) values are lesser, and for low free energy barriers (higher values of ΔG), the log(K_{off}) is higher. We observe such a scenario, especially in the off-target combinations HDAC2-Nafamostat showed a low dissociation rate, and eIF4E2-Nafamostat displayed high dissociation rates. Specifically, for eIF4E2 combinations, the dissociation rates are higher, suggesting the drugs are bound less tightly and have lesser affinities. The HDAC2 and CK2 combinations showed lower ΔG values, indicating more stable and energetically favorable at the bound state. As a result, it will take longer to dissociate from the binding pocket to the solvent crossing the transition barrier.

Pathways and mechanism of drug dissociations from the binding pocket of the host proteins

To explore the complete dissociation pathways from its bound pose and uncover the essential interacting residues that work as gatekeepers facilitating the (dis)association mechanism, we analyzed the crucial interacting residues from the dissociation trajectories for all six combinations. To select the important one from the list of all the residues, we chose a minimum distance cut-off of < 0.3 nm and a normalized probability of 0.8 (see Figure S4-S9). In Table 3, we showed the list of dominant residues for HDAC2 - Nafamostat, eIF4E2 - Nafamostat, eIF4E2 - Camostat, CK2 - Silmitasertib, eIF4E2 – Zotatfin, and HDAC2-Valproic Acid while dissociating from the bound state to the solvent environment. We observed ARG39 (HDAC2-Nafamostat), TRP80 (eIF4E2-Nafamostat), GLU81 (eIF4E2-Camostat), LYS69 and ASP176 (CK2-Silmitasertib), and ARG39

(HDAC2-Valproic Acid) with the highest probability and with a distance cut-off of < 0.2 nm, whereas the residue SER176 (for eIF4E2-Zotatifin) with probability 0.9, distance cut-off < 0.3 nm. In Figure 8 (a-f), we showed instantaneous snapshots of the host protein-ligand binding pocket highlighting the key residues (ligand (orange), residues with probability 1 (yellow), other key residues (lime)). In the case of both HDAC2 combinations, for Nafamostat and Valproic Acid, common residues ARG39, GLY142, LEU144, HIS146, PHE155 were shown to be interacting. Interestingly for eIF4E2 combinations, TRP80 was critical in interactions with all three drugs (Nafamostat, Camostat, and Zotatifin).

Understanding the complete dissociation pathways for a ligand from its bound state and knowledge about the central residues facilitating the (dis)association mechanism is vital in accurate, fast, and effective drug development purposes. To have a rigorous understanding, we analyzed the wt-metaD trajectories of the dissociation events for all the systems. We explored all possible pathways available for a ligand to dissociate from the bound state. In Figure 9 (a-f), we showed instantaneous snapshots for all six systems and all the pathways taken by a specific ligand for a system. For HDAC2 – Nafamostat, we observe two dissociation pathways as shown in Figure 9 (a) (i and ii). Along one path (shown in Figure 9 (a) i), PHE155 works as the gatekeeper while for the other path (Figure 9 (a) ii) HIS183. Out of 10 independent dissociation events, we observed an equal number of possibilities for either pathway or both are equally probable. Hence, PHE155 and HIS183 are key residues facilitating the (dis)association mechanism for the HDAC2-Nafamostat system. For HDAC2-Valproic acid (Figure 9 (b)), the ligand is deeply embedded inside the binding cavity surrounded by ARG39, ILE40, GLY142, LEU144. While dissociating, it reaches the top of the surface and dissociates interacting through PHE155 (Figure 9 (b) i). It also follows two more distinct paths between the helices, one interacting with ILE24, LEU117, GLU113 (Figure 9 (b) ii),

and in another, the ligand reaches the top between LEU276 and PHE155. Then it dissociates interacting with TYR308, ILE310, PHE155, PRO34 (Figure 9 (b) iii). Thus, we observe three distinct pathways for the HDAC2-Valproic acid system. Out of these three pathways, we noticed the path shown in (Figure 9 (b) i) to be statistically more probable for Valproic acid to follow. Hence, for HDAC2, although we observe multiple pathways to be present for Nafamostat and Valproic acid, a single path (Figure 9 (b) i) corresponds to the dissociation of the ligand along PHE155) is conserved for both the ligands. For eIF4E2 – Zotatfin, we observe a single pathway (Figure 9 (c) i) with PRO180 as the gatekeeper residue. For eIF4E2 – Camostat, MET179, THR29, SER30 are at the gateway (pathway Figure 9 (d) i), and GLU81, MET79 at the gateway (for pathway Figure 9 (d) ii). For eIF4E2- Nafamostat (Figure 9 (e)), TRP80, TYR34 residues (pathway Figure 9 (e) i), between helices through TRP80, TYR34 residues (pathway Figure 9 (e) ii), residue ARG94 along with the beta-sheet (pathway Figure 9 (e) iii). Hence, for eIF4E2 for all three ligands, we did not observe any specific pathway common to all three in contrast to HDAC2, where we noticed a conserved path with specific PHE155 residue. For CK2 – Silmitasertib (Figure 9 (f) i), a single pathway has LYS69 and ASP176 as two crucial residues at the gateway. Hence, we explored various dissociation pathways that might be used while ligand associating into the binding cavity and elucidated key interacting residues that facilitate the (dis)association processes for three targets and five different ligands.

Conclusion

With great efforts and difficulty, researchers around the world are looking for better therapeutics to treat SARS-CoV-2. The coronavirus disease COVID-19 has become fatal and has a high transmissibility rate, making it difficult to control the spread. Designing new therapeutic approaches or repurposing existing drugs requires understanding viral pathogenesis or host targets

or pathways that mediate the infection. Various interactome studies have highlighted detailed information on key host regulatory proteins for which repurposed drugs are shown to be effective. It is in line with our previous study, where we have done an exhaustive screening of existing drugs and human targets using molecular docking and free energy calculations. From this study, we were able to filter out potential drug-target combinations that not only have better docking scores, good free energy, and residence time but they are in clinical phase trials. Our current study wanted to extend our previous understanding to describe residue-level details, kinetics, and target-drug (dis)association mechanisms. Such a systematic approach can help us towards a better understanding of host-targeted therapies.

The dissociation of a drug from its binding pocket is a rare event in nature. It occurs in the timescale of microseconds or more and beyond the reach to study using conventional MD simulations. Here, we used enhanced sampling techniques, wt-metaD, to facilitate our understanding of thermodynamics and kinetics of drug-protein interactions. We found the key residues interactions formed in metaD simulations in the bound state. The probability distribution indicates that there is no single well-defined dissociation path. Drugs are diffused in all combinations that have a low dissociation rate. The combinations explore the surface of the target protein by forming metastable states. The HDAC2 have deep concave pockets that maximize the protein-drug interactions. The predominant pathway taken by both HDAC2 combinations is from the catalytic region referred to as a lipophilic tube, which includes the residues PHE155 and HIS183.

Similarly, CK2-Silmaterstib, the residues LYS69, and ASP176 are mediators involved in interaction with the drug molecule. Here we observe LYS69 and ASP176 facilitating the dissociation of the drug. The unbinding process discussed here can involve steps from forming a stable state when the drug is in the binding pocket and then metastable intermediate conformations

where the drug has contact with the extracellular surface of the receptor. The later step constitutes substantial dehydration of the drug and the binding pocket, representing a high energy barrier to an association. The residues involved in each stage can be considered testable cases for further understanding of the mechanism or better therapeutics with better efficiency.

Supporting Information

Table showing the interacting residues of target protein that remain in contact with the respective drug molecules for more than 75% of the simulation time; hydrophobic and $\pi - \pi$ interaction between the ligand-target; minimum distance plot of the protein residues with that of ligand heavy atoms and minimum distance plot with cut-off 0.2 nm; normalized probability distribution with distance cut-off for all six systems.

Acknowledgments

DP thanks the Indian Institute of Technology Kanpur for the postdoctoral fellowship. ABP thanks IITK and Prescience for financial support. DP acknowledges the National Supercomputing Mission (NSM) for providing computing resources of 'PARAM Sanganak' at IIT Kanpur, which is implemented by C-DAC and supported by the Ministry of Electronics and Information Technology (MeitY) and Department of Science and Technology (DST), Government of India. JKS would like to acknowledge SERB, India, for the support.

References

1. Calligari P, Bobone S, Ricci G, Bocedi A. Molecular investigation of SARS–COV-2 proteins and their interactions with antiviral drugs. *Viruses*. 2020;12. doi:10.3390/v12040445
2. Wang L, Wang Y, Ye D, Liu Q. Review of the 2019 novel coronavirus (SARS-CoV-2) based on current evidence. *Int J Antimicrob Agents*. 2020;55. doi:10.1016/j.ijantimicag.2020.105948
3. Grant MC, Geoghegan L, Arbyn M, Mohammed Z, McGuinness L, Clarke EL, et al. The prevalence of symptoms in 24,410 adults infected by the novel coronavirus (SARS-CoV-2; COVID-19): A systematic review and meta-analysis of 148 studies from 9 countries. *PLoS One*. 2020;15. doi:10.1371/journal.pone.0234765
4. Ziebuhr J. Molecular biology of severe acute respiratory syndrome coronavirus. *Current Opinion in Microbiology*. 2004. doi:10.1016/j.mib.2004.06.007
5. Prajapat M, Sarma P, Shekhar N, Prakash A, Avti P, Bhattacharyya A, et al. Update on the target structures of SARS-CoV-2: A systematic review. *Indian Journal of Pharmacology*. 2020. doi:10.4103/ijp.IJP_338_20
6. Shereen MA, Khan S, Kazmi A, Bashir N, Siddique R. COVID-19 infection: Origin, transmission, and characteristics of human coronaviruses. *Journal of Advanced Research*. 2020. doi:10.1016/j.jare.2020.03.005
7. Tan YJ, Lim SG, Hong W. Characterization of viral proteins encoded by the SARS-coronavirus genome. *Antiviral Res*. 2005;65. doi:10.1016/j.antiviral.2004.10.001
8. Ye Y, Hogue BG. Role of the Coronavirus E Viroporin Protein Transmembrane Domain in Virus Assembly. *J Virol*. 2007;81. doi:10.1128/jvi.01472-06
9. Al-Karmalawy AA, Dahab MA, Metwaly AM, Elhady SS, Elkaeed EB, Eissa IH, et al. Molecular Docking and Dynamics Simulation Revealed the Potential Inhibitory Activity of ACEIs Against SARS-CoV-2 Targeting the hACE2 Receptor. *Front Chem*. 2021;9. doi:10.3389/fchem.2021.661230
10. Liu S, Zhu L, Xie G, Mok BW-Y, Yang Z, Deng S, et al. Potential Antiviral Target for SARS-CoV-2: A Key Early Responsive Kinase during Viral Entry. *CCS Chem*. 2021; 559–568. doi:10.31635/ccschem.021.202000603
11. Shastri J, Parikh S, Aggarwal V, Agrawal S, Chatterjee N, Shah R, et al. Severe SARS-CoV-2 Breakthrough Reinfection With Delta Variant After Recovery From Breakthrough Infection by Alpha Variant in a Fully Vaccinated Health Worker. *Front Med*. 2021;8. doi:10.3389/fmed.2021.737007
12. Lindenblatt D, Nickelsen A, Applegate VM, Hochscherf J, Witulski B, Bouaziz Z, et al. Diacritic Binding of an Indenoindole Inhibitor by CK2 α Paralogs Explored by a Reliable Path to Atomic Resolution CK2 α' Structures. *ACS Omega*. 2019;4: 5471–5478.

doi:10.1021/acsomega.8b03415

13. Cruz LR, Baladrón I, Rittoles A, Díaz PA, Valenzuela C, Santana R, et al. Treatment with an Anti-CK2 Synthetic Peptide Improves Clinical Response in COVID-19 Patients with Pneumonia. A Randomized and Controlled Clinical Trial. *ACS Pharmacol Transl Sci.* 2021;4. doi:10.1021/acspsci.0c00175
14. Wagner FF, Weïwer M, Steinbacher S, Schomburg A, Reinemer P, Gale JP, et al. Kinetic and structural insights into the binding of histone deacetylase 1 and 2 (HDAC1, 2) inhibitors. *Bioorganic Med Chem.* 2016;24: 4008–4015. doi:10.1016/j.bmc.2016.06.040
15. Yang F, Zhao N, Ge D, Chen Y. Next-generation of selective histone deacetylase inhibitors. *RSC Adv.* 2019;9: 19571–19583. doi:10.1039/c9ra02985k
16. Clark LK, Green TJ, Petit CM. Structure of Nonstructural Protein 1 from SARS-CoV-2. *J Virol.* 2021;95. doi:10.1128/jvi.02019-20
17. Bouhaddou M, Memon D, Meyer B, White KM, Rezelj V V., Correa Marrero M, et al. The Global Phosphorylation Landscape of SARS-CoV-2 Infection. *Cell.* 2020;182: 685-712.e19. doi:10.1016/j.cell.2020.06.034
18. Bhowmik D, Sharma RD, Prakash A, Kumar D. “Identification of Nafamostat and VR23 as COVID-19 drug candidates by targeting 3CLpro and PLpro.”. *J Mol Struct.* 2021;1233. doi:10.1016/j.molstruc.2021.130094
19. Doi K, Ikeda M, Hayase N, Moriya K, Morimura N, Maehara H, et al. Nafamostat mesylate treatment in combination with favipiravir for patients critically ill with Covid-19: a case series. *Crit Care.* 2020;24: 20–23. doi:10.1186/s13054-020-03078-z
20. Ramakrishnan J, Kandasamy S, Iruthayaraj A, Magudeeswaran S, Chinnasamy K, Poomani K. Strong Binding of Leupeptin with TMPRSS2 Protease May Be an Alternative to Camostat and Nafamostat for SARS-CoV-2 Repurposed Drug: Evaluation from Molecular Docking and Molecular Dynamics Simulations. *Appl Biochem Biotechnol.* 2021;193: 1909–1923. doi:10.1007/s12010-020-03475-8
21. Escalante DE, Ferguson DM. Structural modeling and analysis of the SARS-CoV-2 cell entry inhibitor camostat bound to the trypsin-like protease TMPRSS2. *Med Chem Res.* 2021;30: 399–409. doi:10.1007/s00044-021-02708-7
22. Anand NM, Liya DH, Pradhan AK, Tayal N, Bansal A, Donakonda S, et al. A comprehensive SARS-CoV-2 genomic analysis identifies potential targets for drug repurposing. *PLoS One.* 2021;16: 1–21. doi:10.1371/journal.pone.0248553
23. Behera SK, Vhora N, Contractor D, Shard A, Kumar D, Kalia K, et al. Computational drug repurposing study elucidating simultaneous inhibition of entry and replication of novel corona virus by Grazoprevir. *Sci Rep.* 2021;11: 1–11. doi:10.1038/s41598-021-86712-2
24. Carino A, Moraca F, Fiorillo B, Marchianò S, Sepe V, Biagioli M, et al. Hijacking SARS-CoV-2/ACE2 receptor interaction by natural and semi-synthetic steroidal agents acting on

- functional pockets on the receptor binding domain. *Front Chem.* 2020;8: 1–15. doi:10.3389/fchem.2020.572885
25. Hempel T, Raich L, Olsson S, Azouz NP, Klingler AM, Hoffmann M, et al. Molecular mechanism of inhibiting the SARS-CoV-2 cell entry facilitator TMPRSS2 with camostat and nafamostat. *Chem Sci.* 2021;12. doi:10.1039/d0sc05064d
 26. Kumawat A, Namsani S, Pramanik D, Roy S, Singh JK. Integrated docking and enhanced sampling-based selection of repurposing drugs for SARS-CoV-2 by targeting host dependent factors. *J Biomol Struct Dyn.* 2021. doi:10.1080/07391102.2021.1937319
 27. PRinS3, Version v1.0.0, Release 2021, Prescience Insilico Pvt. Ltd., India. 2021.
 28. Sixto-López Y, Bello M, Correa-Basurto J. Exploring the inhibitory activity of valproic acid against the HDAC family using an MMGBSA approach. *J Comput Aided Mol Des.* 2020;34: 857–878. doi:10.1007/s10822-020-00304-2
 29. Tiwary P, Limongelli V, Salvalaglio M, Parrinello M. Kinetics of protein-ligand unbinding: Predicting pathways, rates, and rate-limiting steps. *Proc Natl Acad Sci U S A.* 2015;112: E386–E391. doi:10.1073/pnas.1424461112
 30. Sauvat A, Ciccocanti F, Colavita F, Di Rienzo M, Castilletti C, Capobianchi MR, et al. On-target versus off-target effects of drugs inhibiting the replication of SARS-CoV-2. *Cell Death Dis.* 2020;11. doi:10.1038/s41419-020-02842-x
 31. Morris GM, Ruth H, Lindstrom W, Sanner MF, Belew RK, Goodsell DS, et al. Software news and updates AutoDock4 and AutoDockTools4: Automated docking with selective receptor flexibility. *J Comput Chem.* 2009;30. doi:10.1002/jcc.21256
 32. Webb B, Sali A. Comparative protein structure modeling using MODELLER. *Curr Protoc Bioinforma.* 2016;2016. doi:10.1002/cpbi.3
 33. Harris R, Olson AJ, Goodsell DS. Automated prediction of ligand-binding sites in proteins. *Proteins Struct Funct Genet.* 2008;70. doi:10.1002/prot.21645
 34. Abraham MJ, Murtola T, Schulz R, Páll S, Smith JC, Hess B, et al. Gromacs: High performance molecular simulations through multi-level parallelism from laptops to supercomputers. *SoftwareX.* 2015;1–2. doi:10.1016/j.softx.2015.06.001
 35. MacKerell AD, Banavali N, Foloppe N. Development and current status of the CHARMM force field for nucleic acids. *Biopolymers.* 2000;56. doi:10.1002/1097-0282(2000)56:4<257::AID-BIP10029>3.0.CO;2-W
 36. Frisch MJ, Trucks GW, Schlegel HB, Scuseria GE, Robb MA, Cheeseman JR, et al. Gaussian 09, Revision A. 02; Gaussian, Inc: Wallingford, CT, 2009. There is no Corresp Rec this Ref. 2015.
 37. Zoete V, Cuendet MA, Grosdidier A, Michielin O. SwissParam: A fast force field generation tool for small organic molecules. *J Comput Chem.* 2011;32. doi:10.1002/jcc.21816

38. Breneman CM, Wiberg KB. Determining atom-centered monopoles from molecular electrostatic potentials. The need for high sampling density in formamide conformational analysis. *J Comput Chem*. 1990;11. doi:10.1002/jcc.540110311
39. Bussi G, Donadio D, Parrinello M. Canonical sampling through velocity rescaling. *J Chem Phys*. 2007;126: 014101. doi:10.1063/1.2408420
40. Parrinello M, Rahman A. Polymorphic transitions in single crystals: A new molecular dynamics method. *J Appl Phys*. 1981;52: 7182–7190. doi:10.1063/1.328693
41. Essmann U, Perera L, Berkowitz ML, Darden T, Lee H, Pedersen LG. A smooth particle mesh Ewald method. *J Chem Phys*. 1995;103: 8577–8593. doi:10.1063/1.470117
42. Hess B, Bekker H, Berendsen HJC, Fraaije JGEM. LINCS: A Linear Constraint Solver for molecular simulations. *J Comput Chem*. 1997;18. doi:10.1002/(SICI)1096-987X(199709)18:12<1463::AID-JCC4>3.0.CO;2-H
43. ProLIF (Protein-Ligand Interaction Fingerprints).
44. Smith Z, Pramanik D, Tsai ST, Tiwary P. Multi-dimensional spectral gap optimization of order parameters (SGOOP) through conditional probability factorization. *J Chem Phys*. 2018;149. doi:10.1063/1.5064856
45. Pramanik D, Smith Z, Kells A, Tiwary P. Can One Trust Kinetic and Thermodynamic Observables from Biased Metadynamics Simulations?: Detailed Quantitative Benchmarks on Millimolar Drug Fragment Dissociation. *J Phys Chem B*. 2019;123. doi:10.1021/acs.jpcb.9b01813
46. Tiwary P. Molecular Determinants and Bottlenecks in the Dissociation Dynamics of Biotin-Streptavidin. *J Phys Chem B*. 2017;121: 10841–10849. doi:10.1021/acs.jpcb.7b09510
47. Ribeiro JML, Tsai ST, Pramanik D, Wang Y, Tiwary P. Kinetics of Ligand-Protein Dissociation from All-Atom Simulations: Are We There Yet? *Biochemistry*. 2019. doi:10.1021/acs.biochem.8b00977
48. Laio A, Parrinello M. Escaping free-energy minima. *Proc Natl Acad Sci*. 2002;99: 12562–12566. doi:10.1073/PNAS.202427399
49. Barducci A, Bussi G, Parrinello M. Well-Tempered Metadynamics: A Smoothly Converging and Tunable Free-Energy Method. *Phys Rev Lett*. 2008;100: 020603. doi:10.1103/PhysRevLett.100.020603
50. Bonomi M, Branduardi D, Bussi G, Camilloni C, Provasi D, Raiteri P, et al. PLUMED: A portable plugin for free-energy calculations with molecular dynamics. *Comput Phys Commun*. 2009;180. doi:10.1016/j.cpc.2009.05.011
51. Namsani S, Pramanik D, Khan MA, Roy S, Singh JK. Metadynamics-based enhanced sampling protocol for virtual screening: case study for 3CLpro protein for SARS-CoV-2. *J Biomol Struct Dyn*. 2021. doi:10.1080/07391102.2021.1892530

Table 1. The host target protein and drug combinations studied in this paper, and their role of specific pathways involved in host cells.

Target	Pathway	Structure (PDB ID)	Drug
eIF4E2	Translation	2JGB	Nafamostat
eIF4E2	Translation	2JGB	Camostat
eIF4E2	Translation	2JGB	Zotatifin
HDAC2	Epigenetic factor	4LY1	Nafamostat
HDAC2	Epigenetic factor	4LY1	Valproic acid
CSK22	Transcription	6HMB	Silmitasertib

Table 2: Average free energy barriers[26] and dissociation rates are shown for six target – drug combinations.

Target	Drug	ΔG (kcal/mol)	K_{off} (1/min)
eIF4E2	Nafamostat	-4.3 (0.31)	1.3E-04
eIF4E2	Camostat	-3.3 (0.34)	1.3E-02
eIF4E2	Zotatifin	-3.5 (0.31)	5.6E+00
HDAC2	Nafamostat	-13.3 (0.45)	2.3E-09

HDAC2	Valproic acid	-12.8 (0.34)	7.7E-11
CK2	Silmitasertib	-8.6 (0.56)	7.7E-10

Table 3: List of target protein residues interacting with the ligand from metadynamics simulations from 10 independent runs for each system. The target residues having probability of $\geq 80\%$ and with the distance < 0.3 nm have been chosen. The table shows interaction sites and corresponding protein residues of the target for HDAC2 - Nafamostat, eIF4E2 - Nafamostat, eIF4E2 - Camostat, CSK22 - Silmitasertib, eIF4E2 – Zotatfin and HDAC2-Valproic acid for dissociation pathways.

Target	PDB ID	Drug	Interacting Residues
eIF4E2	2JGB	Nafamostat	TYR34, TRP80, LYS90, ARG94, SER128
eIF4E2	2JGB	Camostat	THR29, SER30, MET79, TRP80, GLU81, ARG130, MET179
eIF4E2	2JGB	Zotatfin	SER30, SER31, TRP80, SER176, PRO180, ARG187
HDAC2	4LY1	Nafamostat	ARG39, GLY142, LEU144, HIS146, GLY154, PHE155, CYS156, HIS183, GLY306
HDAC2	4LY1	Valproic Acid	ARG39, ILE40, GLY142, LEU144, HIS146, PHE155, LEU276

CSK22	6HMB	Silmitasertib	GLY47, ARG48, GLY49, SER52, VAL54, LYS69, GLU82, LEU86, ILE96, LYS159, MET164, ASP176, SER195
-------	------	---------------	--

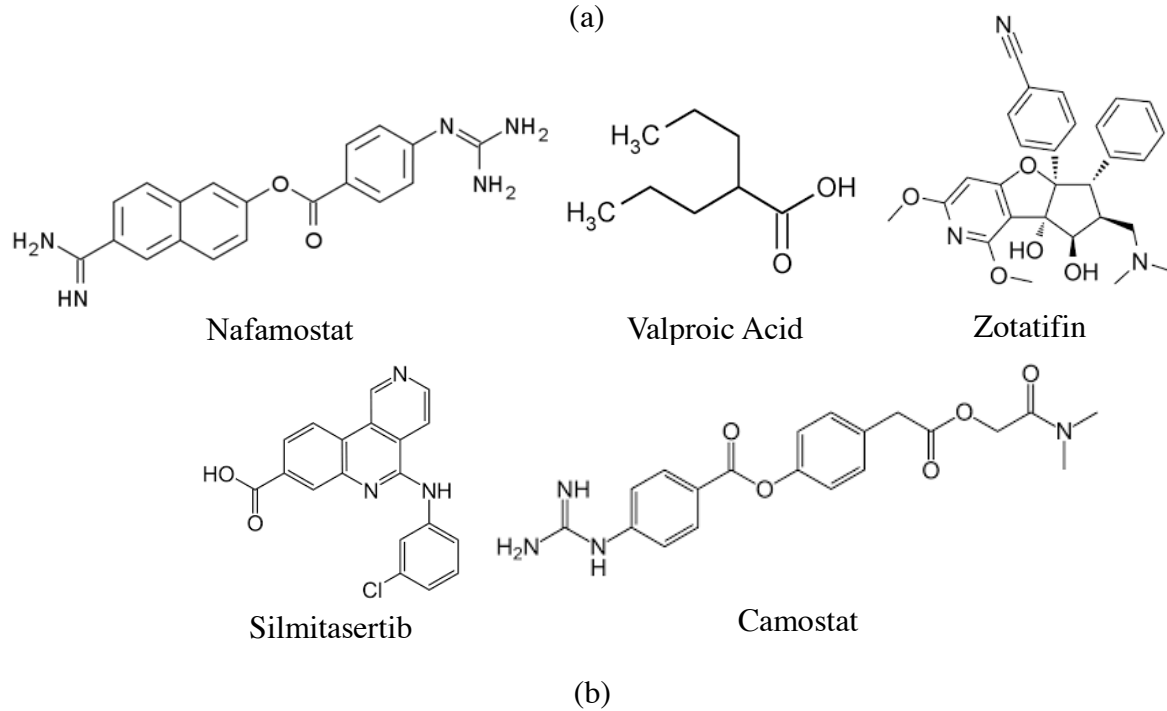
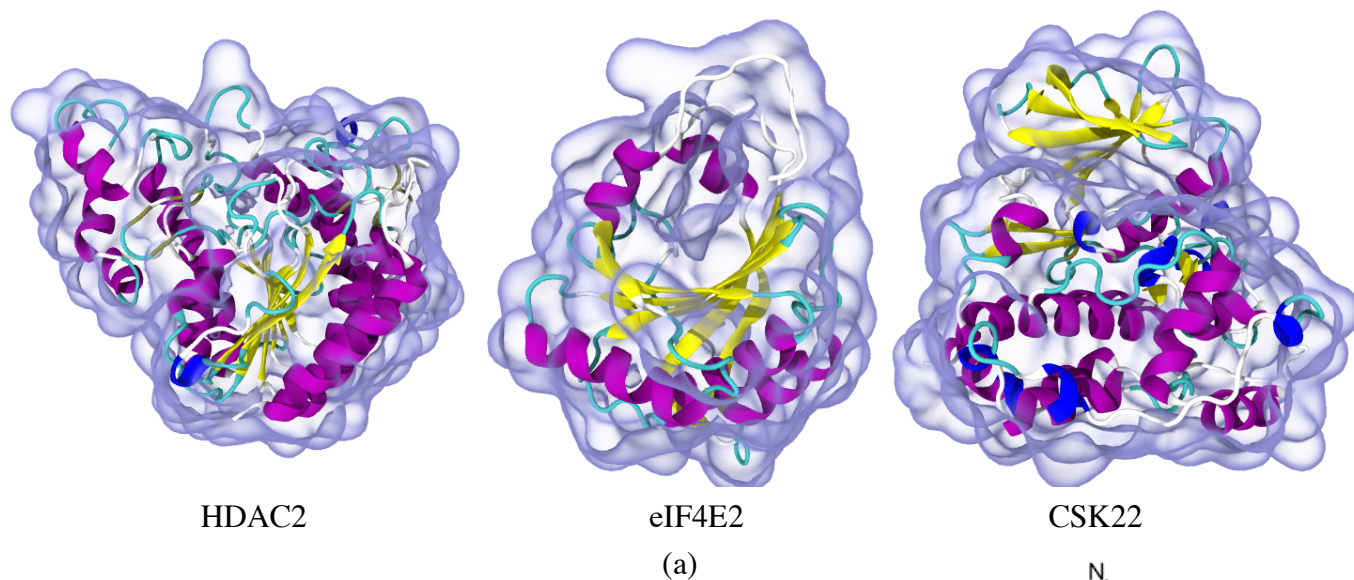


Figure 1: (a) Instantaneous snapshots of the secondary structures of HDAC2, eIF4E2 and CSK22 protein targets. (b) 2D chemical structures of Nafamostat, Valproic acid, Zotatiffin, Silmitasertib and Camostat.

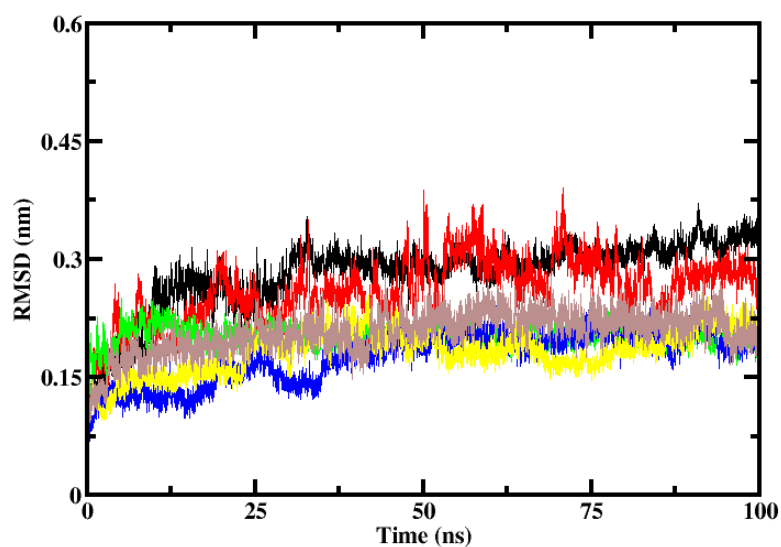


Figure 2: Root mean square deviation of target eIF4E2 complexed to different drugs Nafamostat (black), Camostat (red), Zotatiffin (green), target HDAC2 complexed to Nafamostat (blue), Valproic acid (yellow) and target CSK22 Silmitasertib (brown)

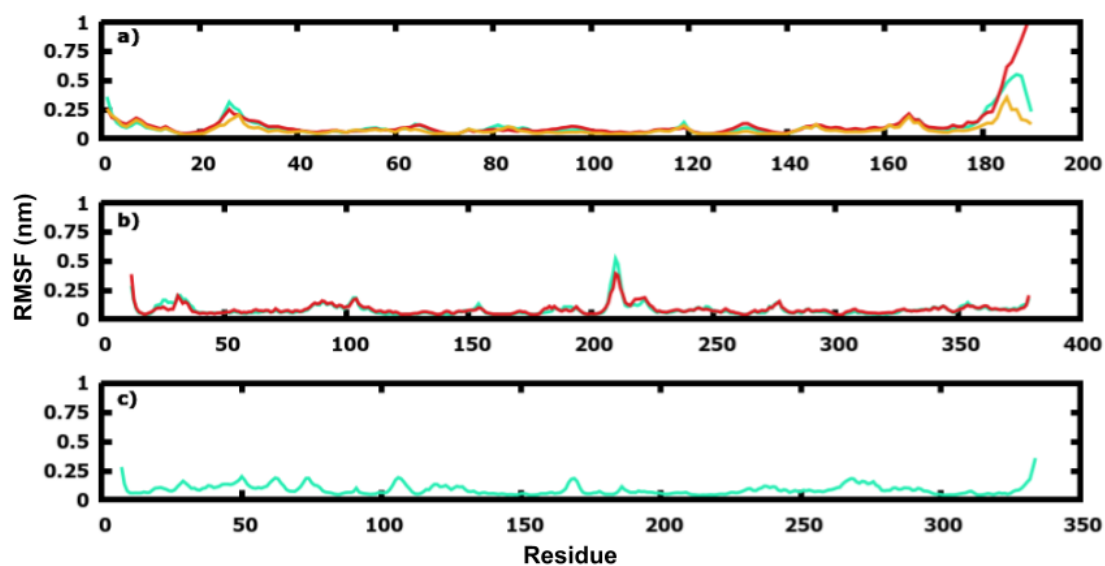


Figure 3: Root mean square fluctuation of protein backbone (a) eIF4E complexed to drug Nafamostat (cyan), Camostat (red), Zotatiffin (orange) (b) HDAC2 complexed to Nafamostat (cyan), Valproic acid (red) (c) CSK22 complexed to Silmitasertib (cyan)

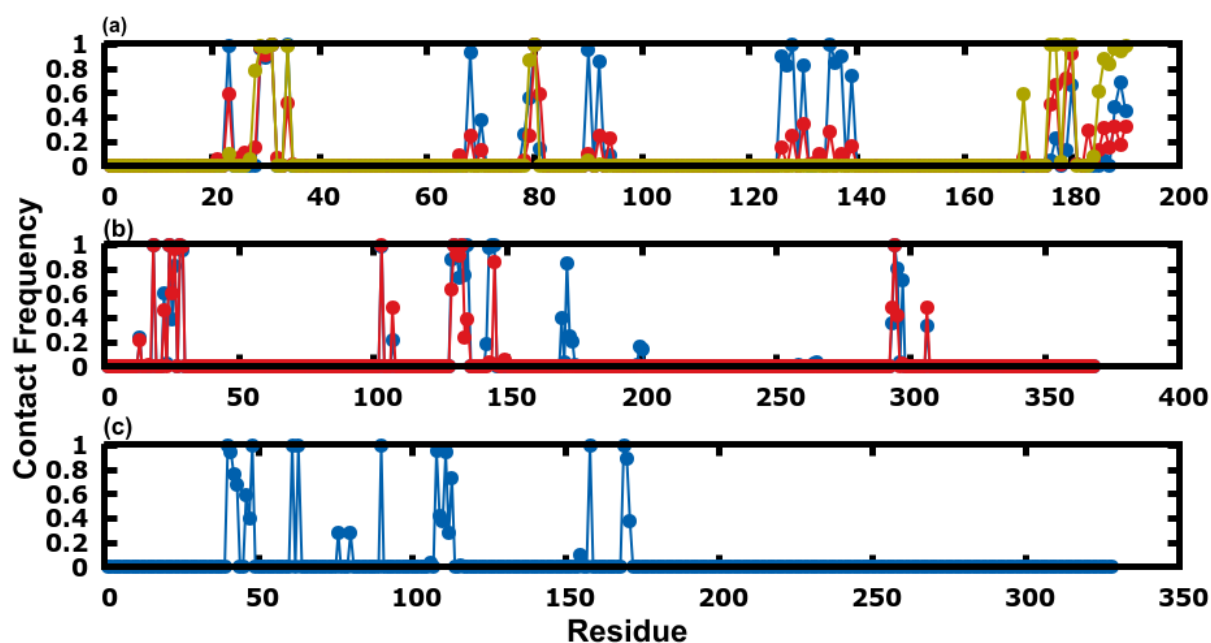


Figure 4: Contact frequency of the drug bound to target protein was calculated for (a) eIF4E – Nafamostat (blue), Camostat (red) and Zotatiffin (orange) (b) HDAC2 – Nafamostat (blue), Valproic acid (red) (c) CSK22 - Silmitasertib (blue)

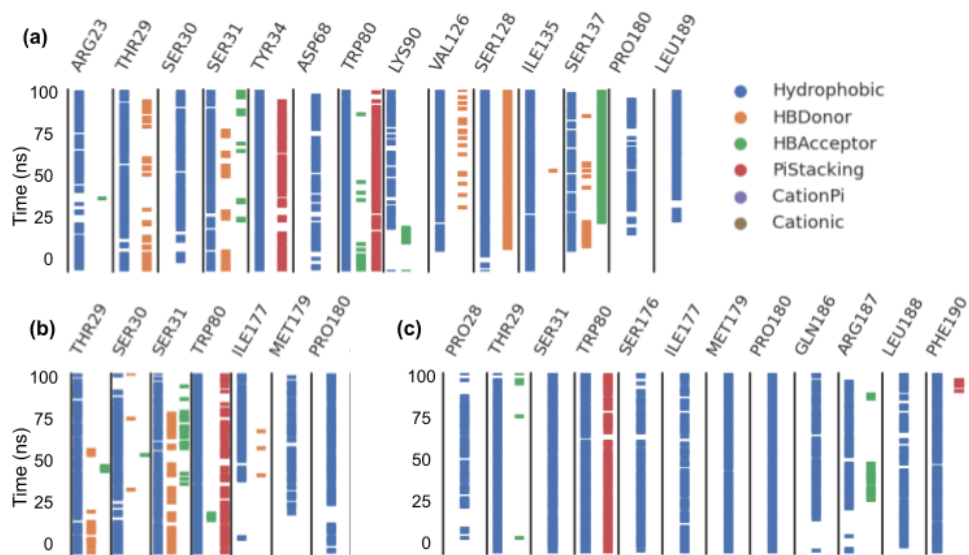


Figure 5: Interaction fingerprint for (a) eIF4E - Nafamostat (b) eIF4E - Camostat (c) eIF4E – Zotatfin

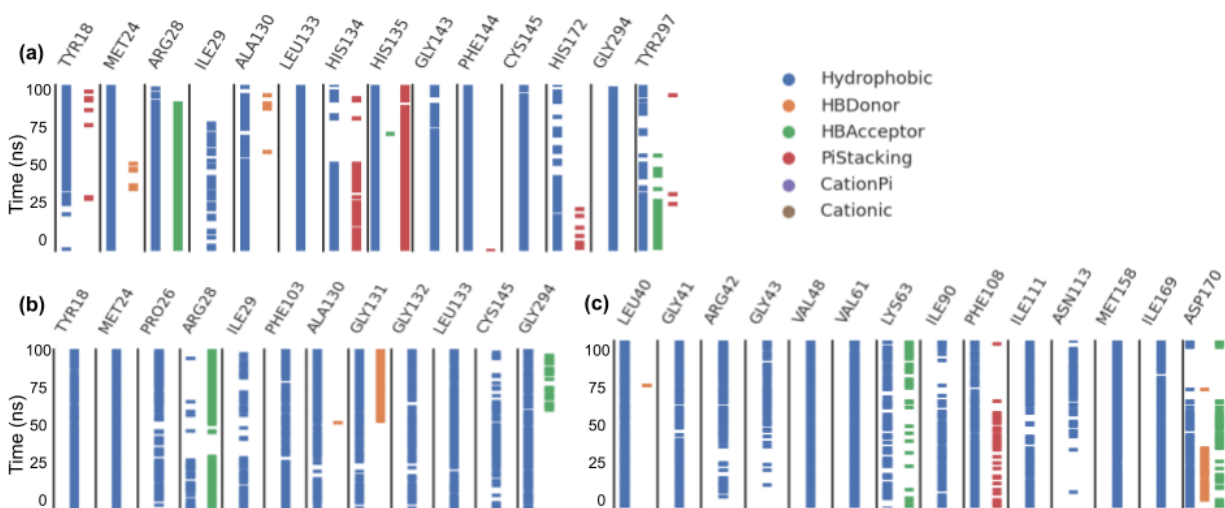


Figure 6: Interaction fingerprint for (a) HDAC2 – Nafamostat (b) HDAC2 - Valproic acid (c) CSK22 - Silmitasertib

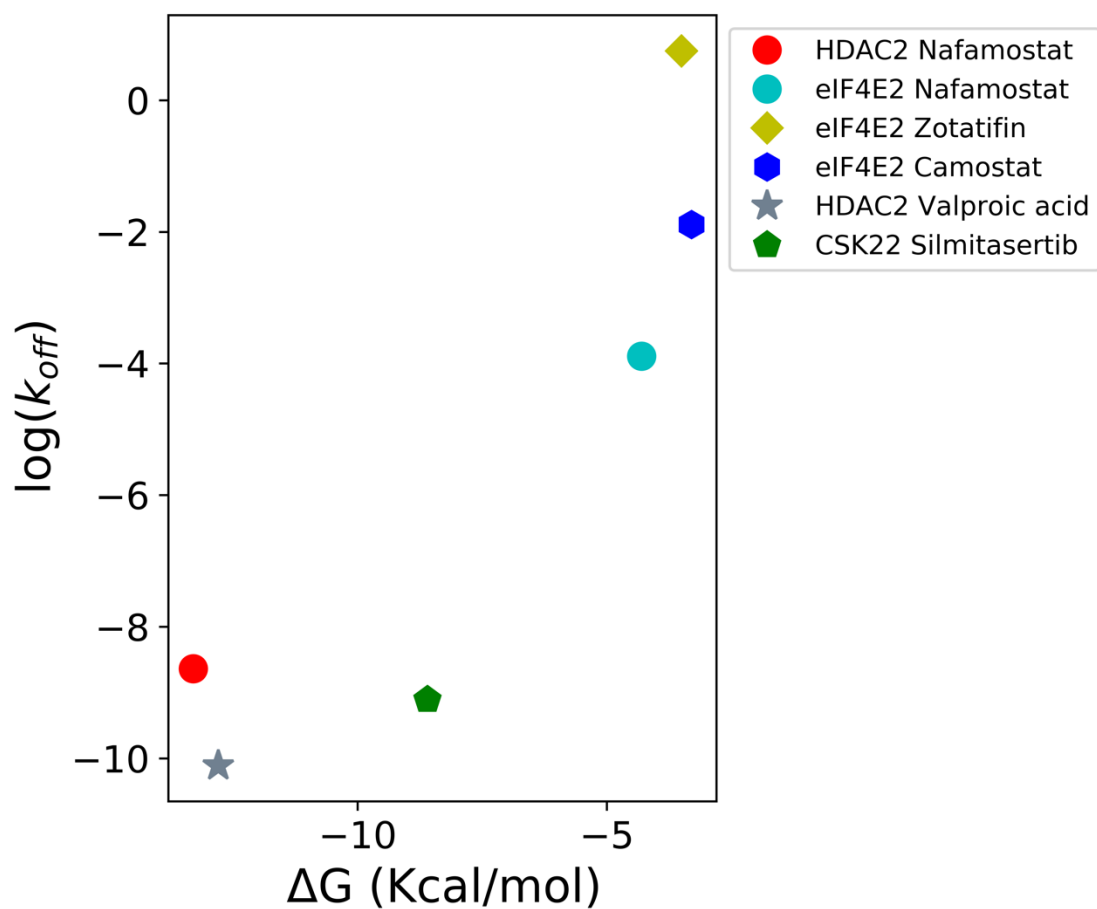


Figure 7: ' $\log(K_{off})$ ' vs 'free energy barrier' has been plotted here for various target - ligand combinations as shown by separate colors and symbols. Different drugs have been shown in separate symbols.

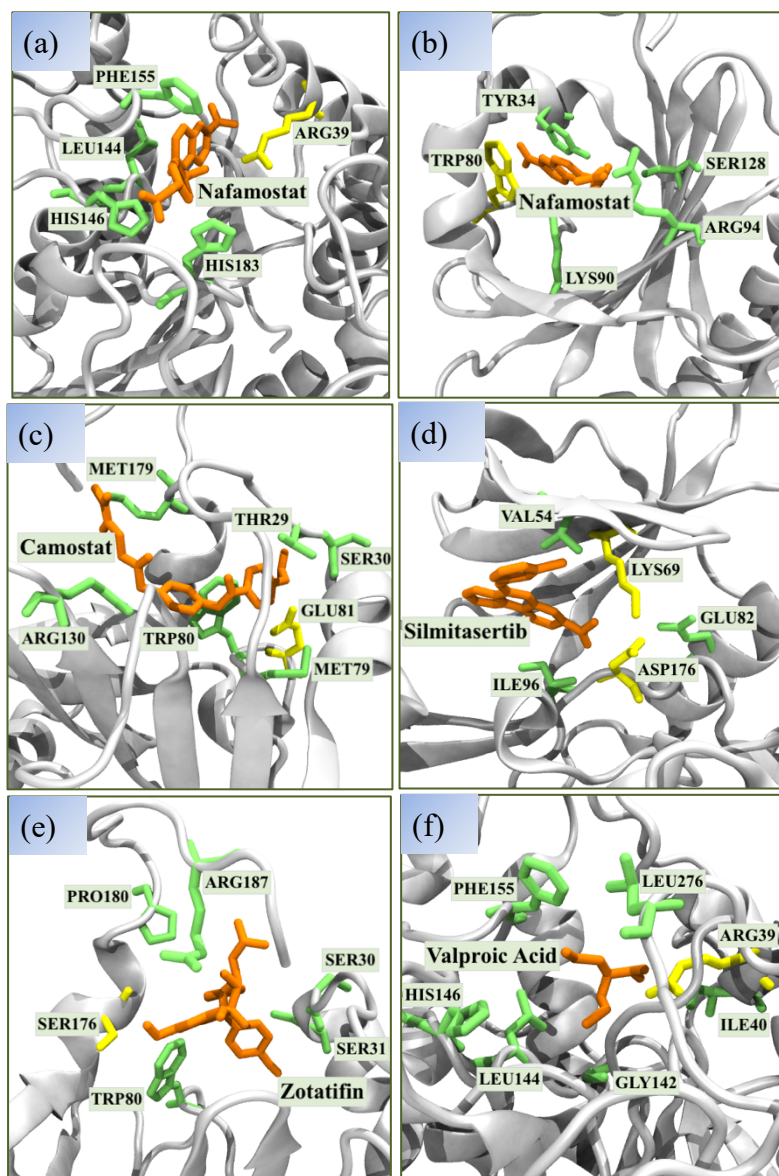
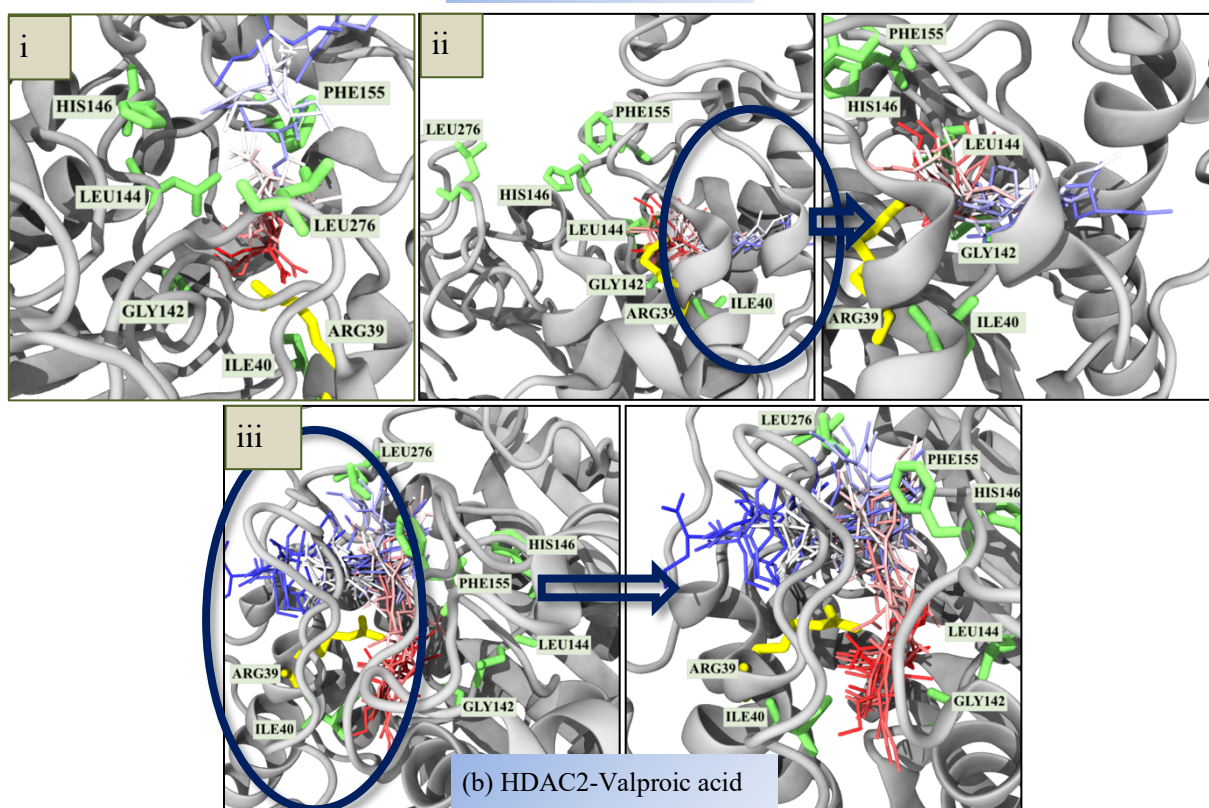
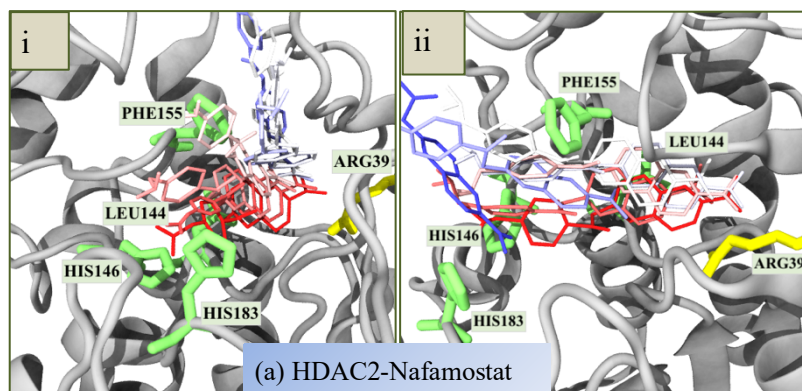


Figure 8: Interacting residues having probability more than 80 % and distance < 0.3 nm for six systems. Orange colors show ligands, yellow residues with probability 1 and lime colors are with probability > 0.8 and distance < 0.3 nm. (a) HDAC2 - Nafamostat, (b) eIF4E2 – Nafamostat, (c) eIF4E2 – Camostat, (d) CSK22 – Silmitasertib, (e) eIF4E2 – Zotatfin, (f) HDAC2 – Valproic Acid.



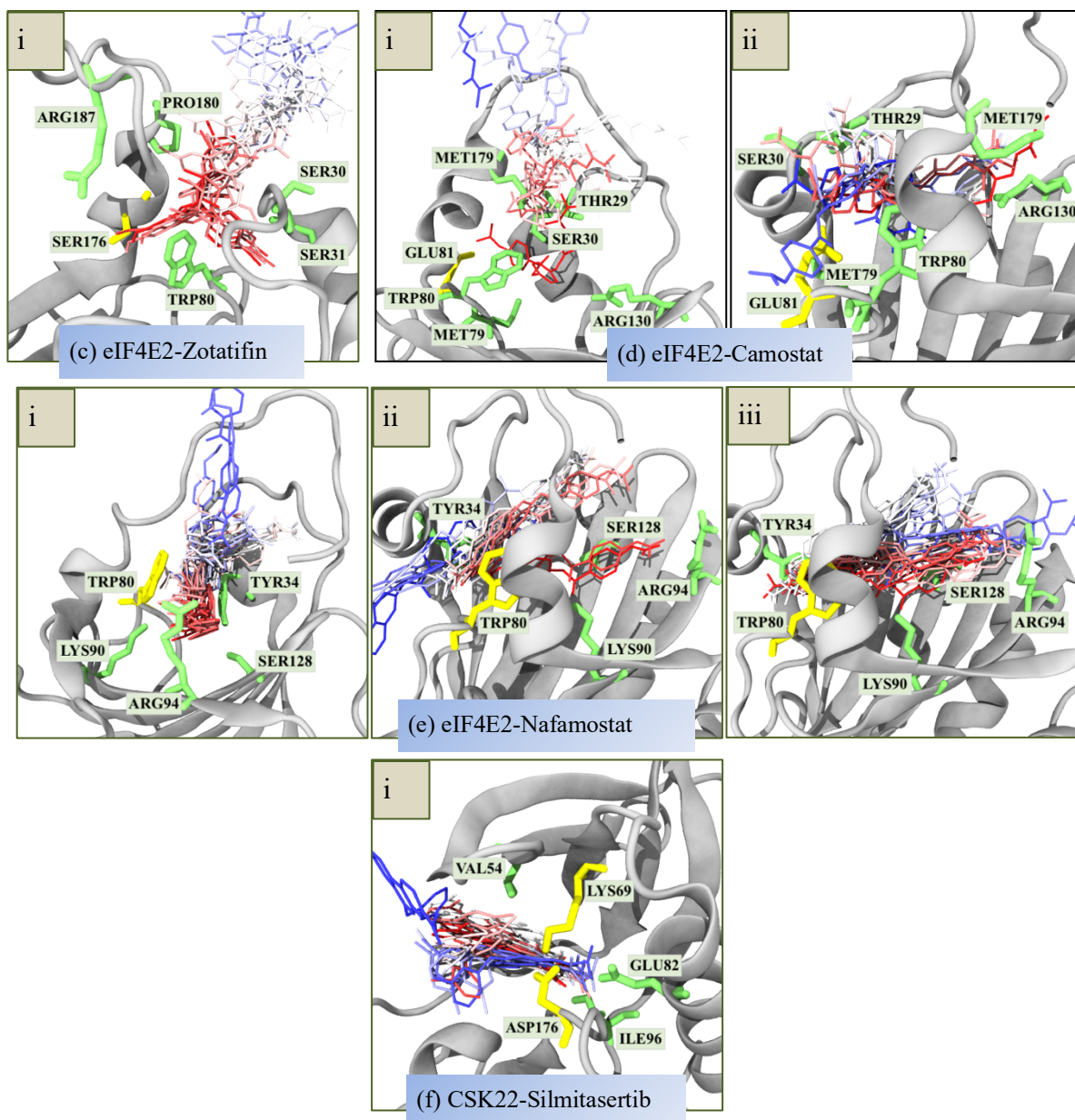


Figure 9: Dissociation pathways for (a) HDAC2 – Nafamostat (i and ii), (b) HDAC2 - Valproic acid (i, ii and iii), (c) eIF4E2 – Zotatiffin (i), (d) eIF4E2 – Camostat (i and ii), (e) eIF4E2 –

Nafamostat (i, ii and iii), (f) CSK22 – Silmitasertib (i). The time evolution of the dissociation events for the ligands have been shown in Timestep representation with Licorice drawing method and the colors denote: red (bound state) → pink → white → light blue → blue (unbound state).